Tropical Cyclone Interaction with the Ocean: The Role of High-Frequency (Subdaily) Coupled Processes

ENRICO SCOCCIMARRO

Istituto Nazionale di Geofisica e Vulcanologia, and Fondazione Centro Euro-Mediterraneo sui Cambiamenti Climatici, Bologna, Italy

PIER GIUSEPPE FOGLI

Fondazione Centro Euro-Mediterraneo sui Cambiamenti Climatici, Bologna, Italy

KEVIN A. REED

School of Marine and Atmospheric Sciences, Stony Brook University, Stony Brook, New York

SILVIO GUALDI, SIMONA MASINA, AND ANTONIO NAVARRA

Istituto Nazionale di Geofisica e Vulcanologia, and Fondazione Centro Euro-Mediterraneo sui Cambiamenti Climatici, Bologna, Italy

ABSTRACT

Through tropical cyclone (TC) activity the ocean and the atmosphere exchange a large amount of energy. In this work possible improvements introduced by a higher coupling frequency are tested between the two components of a climate model in the representation of TC intensity and TC–ocean feedbacks. The analysis is based on the new Centro Euro-Mediterraneo per I Cambiamenti Climatici Climate Model (CMCC-CM2-VHR), capable of representing realistic TCs up to category-5 storms. A significant role of the negative sea surface temperature (SST) feedback, leading to a weakening of the cyclone intensity, is made apparent by the improved representation of high-frequency coupled processes. The first part of this study demonstrates that a more realistic representation of strong TC count is obtained by coupling atmosphere and ocean components at hourly instead of daily frequency. Coherently, the positive bias of the annually averaged power dissipation index associated with TCs is reduced by one order of magnitude when coupling at the hourly frequency, compared to both forced mode and daily coupling frequency results. The second part of this work shows a case study (a modeled category-5 typhoon) analysis to verify the impact of a more realistic representation of the high-frequency coupling in representing the TC effect on the ocean; the theoretical subsurface warming induced by TCs is well represented when coupling the two components at the higher frequency. This work demonstrates that an increased horizontal resolution of model components is not sufficient to ensure a realistic representation of intense and fast-moving systems, such as tropical and extratropical cyclones, but a concurrent increase in coupling frequency is required.

1. Introduction

Tropical cyclone (TC) activity has a significant role in the exchange of energy between the atmosphere and the ocean (Bueti et al. 2014). The variability of the upper-ocean temperature modulates TC intensity (Emanuel et al. 2004), but TC activity also has a role in the modulation of the thermal and dynamical structure of the ocean (Emanuel 2001). Two feedbacks between the atmosphere and the ocean are associated with TC development. The first one is a positive feedback, and it is associated with the induced increase of the latent heat from the ocean into the atmosphere and thus to an increase of the energy available for TC development. The second is a negative feedback resulting from the cooling of the sea surface,

mainly driven by the cold water upwelling induced by the divergence at the ocean surface associated with the wind stress, and also to the shear-induced mixing at the base of the mixed layer (Sriver et al. 2010). This cooling is reflected in a reduction of the heat flux from the ocean into the atmosphere leading to a weakening of the TC. This cooling effect is a function of the prestorm ocean condition, TC intensity, TC traveling speed, and TC size (Huang et al. 2015). TC intensification is suppressed by strong ocean stratification since it favors large sea surface temperature (SST) cooling, and the tendency of tropical cyclones to intensify is less inhibited when stratification is weak (Lloyd and Vecchi 2011). Thus, changes in oceanic stratification modulate the amplitude of TC-induced cooling and hence the negative feedback of air–sea interactions on the TC intensity (Vincent et al. 2014). In addition, changes in projected ocean stratification are expected to reduce the amount of increase in TC intensity with warming (Huang et al. 2015; Emanuel 2015).

Very few CMIP5 models demonstrated ability in representing TCs, mainly because of their coarse horizontal resolution (Camargo 2013). Recent work also suggests a dependency of the TC representation on the convective schemes and dynamical cores adopted (Camargo 2013; Reed et al. 2015). The modeled energy input by the winds into the ocean is primarily dependent on the resolution of the atmospheric component and on the coupling frequency. Increasing the coupling frequency between the atmosphere and ocean components of a general circulation model (GCM) also improves the representation of the feedback induced by the cold wake created by TCs.

Previous studies, performed with GCMs at relatively low horizontal resolutions (hundreds of kilometers) suggested that by increasing the frequency of coupling, the density of TC activity tends to decrease, at least over some basins (Daloz et al. 2012). A realistic atmosphere–ocean interaction is also important when simulating TC activity under different climate conditions (Bell et al. 2013). Here, we aim to investigate TC–ocean interaction through the new GCM developed at the Centro Euro-Mediterraneo per I Cambiamenti Climatici in its higher-horizontal-resolution version (CMCC-CM2-VHR). The model is a fully coupled GCM, with a horizontal resolution of ¼° in both atmospheric and ocean components. The model is capable of realistically representing TCs up to category (cat) 5, following the Saffir–Simpson scale, similar to what has been obtained recently by the GFDL High-Resolution Forecast-Oriented Low Ocean Resolution (HiFLOR) coupled model (Murakami et al. 2015) and the Community Earth System Model (CESM; Small et al. 2014) using the same horizontal resolution in their atmospheric component.

In this work we want to answer the following question: Since the ocean supplies the necessary energy for the development and intensification of TCs (Huang et al. 2015), to what extent does the SST negative feedback affect TC intensity? To answer this question, we test the effect of using different coupling frequencies in determining the ability of the CMCC-CM2-VHR to represent TC activity. In addition, potential TC effects on the ocean, appearing when coupling atmosphere and ocean components at high (hourly) frequency, are investigated.

The paper is organized as follows: Section 2 describes the climate model used, the experiment design, the TC tracking method, and the observational datasets used to validate model results. Section 3 describes TC statistics obtained in the performed experiments, while section 4 deeply investigates a simulated cat-5 typhoon case study. Section 5 discusses the main results and concludes the paper.

2. Data and methodology

a. Model and simulations

The Centro Euro-Mediterraneo sui Cambiamenti Climatici Climate Model, version 2 with very high resolution (CMCC-CM2-VHR), used in this work is the highest-resolution version of the fully coupled CMCC-CM2 model, which represents the physical core of the new CMCC Earth system model (Fogli and Iovino 2014). The ocean component is based on version 3.4 of the NEMO ocean general circulation model (Madec et al. 2008) and has a horizontal resolution of ¼° with 50 vertical levels (22 levels representing the upper 100 m). The atmospheric component is the Community Atmosphere Model, version 5 (CAM5; Hurrell et al. 2013), with a horizontal resolution of ¼° and 30 vertical levels. This study uses the finite-volume dynamical core, as this implementation of the model numerics appears to provide reasonable simulation of TC intensity (Wehner et al. 2014; Reed and Jablonowski 2012; Reed et al. 2015; Bacmeister et al. 2014). The sea ice component, implemented over the same horizontal grid of the ocean model, is the Community Ice Code, version 4 (CICE4; Hunke and Lipscomb 2008). The land component is the Community Land Model, version 4.0 (CLM4.0; Lawrence et al. 2011; Oleson et al. 2010), which uses the same horizontal grid of the atmospheric model. All the components are synchronized by the CESM coupler/driver (cpl7) (Craig et al. 2012), which is also responsible for the exchange of energy, mass, and momentum fluxes between the different components. In the current configuration of the model, the coupling frequency is identical for atmosphere, land, and sea ice components (15 min), while the coupling to the ocean can use the same frequency or a multiple. It is worth noting that

since the atmosphere and ocean components both operate on a horizontal resolution of $\frac{1}{4}°$, potential issues related to coupling grids of various resolutions (Zarzycki et al. 2016) are avoided.

Three 2-yr present-day climate simulations have been performed using the CMCC-CM2-VHR:

1) an atmospheric simulation forced with present-day SST (FORCED; i.e., 1981–2000 climatological conditions both in terms of SST and radiative forcings);
2) a fully coupled simulation, where the ocean is coupled to the atmosphere at low frequency (every 24 h) and radiative forcing conditions are averages over the 1981–2000 period (LF); and
3) a fully coupled simulation, where the ocean is coupled to the atmosphere at high frequency (every 1.5 h), with the same radiative forcing conditions used in the LF simulation (HF).

The radiative forcing used, in terms of greenhouse gases, aerosols, ozone, and solar radiation, represents the present-day period (1981–2000) in all the simulations. After a 1-yr spinup, because of the high computational cost, we were only able to simulate 6 yr of present-day climate: 2 yr in FORCED mode, 2 yr in LF configuration, and 2 yr in HF configuration. Such a short time period is not sufficient to provide an extensive evaluation of the model performances in representing TC interannual variability, but the number of TC conditions (as defined in section 2b) obtained is sufficient to ensure the significance of the results found: 161, 175, and 142 TCs are found in the FORCED, LF, and HF simulations, considering 4382, 4688, and 3916 TC conditions every 6 h, respectively.

The analyses have been performed using 6-hourly atmospheric and ocean model outputs. The TC detection (see section 2b) is based on atmospheric 6-hourly snapshots, and only the 10-m wind module field (U10) is considered as the maximum value reached within the 6-hourly time step. Since the atmospheric model has a time step on the order of 1 min, this value is comparable to the "1 min sustained wind" adopted by the U.S. National Weather Service to define sustained winds within tropical cyclones and to classify them based on their wind intensity.

To better highlight the role of the coupling frequency in representing the TC–ocean interaction, a case study is also shown: the most intense TC (a category-5 typhoon in the western North Pacific occurred at the beginning of July within the first year of the LF simulation) has been simulated using the HF setup, starting from the same LF configuration 1 July initial condition. When comparing LF and HF results for the case study (section 4), 6-hourly averages have been used for both ocean and atmospheric fields.

b. Simulated occurrence of TCs: Detection method

An overview of the criteria adopted for TC detection in atmospheric analyses and model simulations is given in a series of papers carried out within the World Climate Research Programme (WCRP) Tropical Cyclone Intercomparison Project (TCMIP; Walsh et al. 2013) and the U.S. CLIVAR Hurricane Working Group (Scoccimarro et al. 2014; Horn et al. 2014; Villarini et al. 2014; Walsh et al. 2015).

The occurrence method used in this work is a tracking technique looking for individual TCs based on objective criteria for the identification of specific atmospheric conditions based on Zhao et al. (2009). In particular, a two-step procedure is applied:

1) Potential storms are identified based on the three following criteria:
   (i) For each 6-h time step, the grid points where the relative vorticity at 850 hPa exceeds the threshold of $1.6 \times 10^{-4}\,\text{s}^{-1}$ are identified.
   (ii) If a local sea level pressure minimum is located within a distance of 2° latitude or longitude from the vorticity maximum defined in the previous criterion, the relative grid point is considered as the center of the storm. In addition, the local maximum of the 10-m wind speed within the 6-h step is recorded.
   (iii) The TC warm core is defined based on the temperature averaged between 300 and 500 hPa. Only a warm-core temperature greater than 1°C with respect to the surrounding mean temperature (over a 6° latitude × 6° longitude box) is considered as associated with a TC condition. The distance of the warm-core center from the storm center must be within 2°.
2) Storms are tracked as follows: for each potential storm condition, the algorithm verifies the presence of storms during the following 6-h time period within a distance of 400 km. If no storm is found, the trajectory is considered finished. If any storm is detected, the closest storm is chosen as belonging to the same trajectory as the initial storm. To qualify a tracked trajectory as a storm, it must last at least 3 days and have a maximum surface wind speed greater than $17\,\text{m s}^{-1}$ during at least 3 days, without any constraint regarding their timing during the TC evolution.

This tracking algorithm has been validated as capable of realistically representing TC activity in previous studies (Reed et al. 2015; Bacmeister et al. 2016) based on stand-alone atmospheric simulations using an atmospheric component very similar to the one we use here, both in terms of parameterizations and spatial resolution.
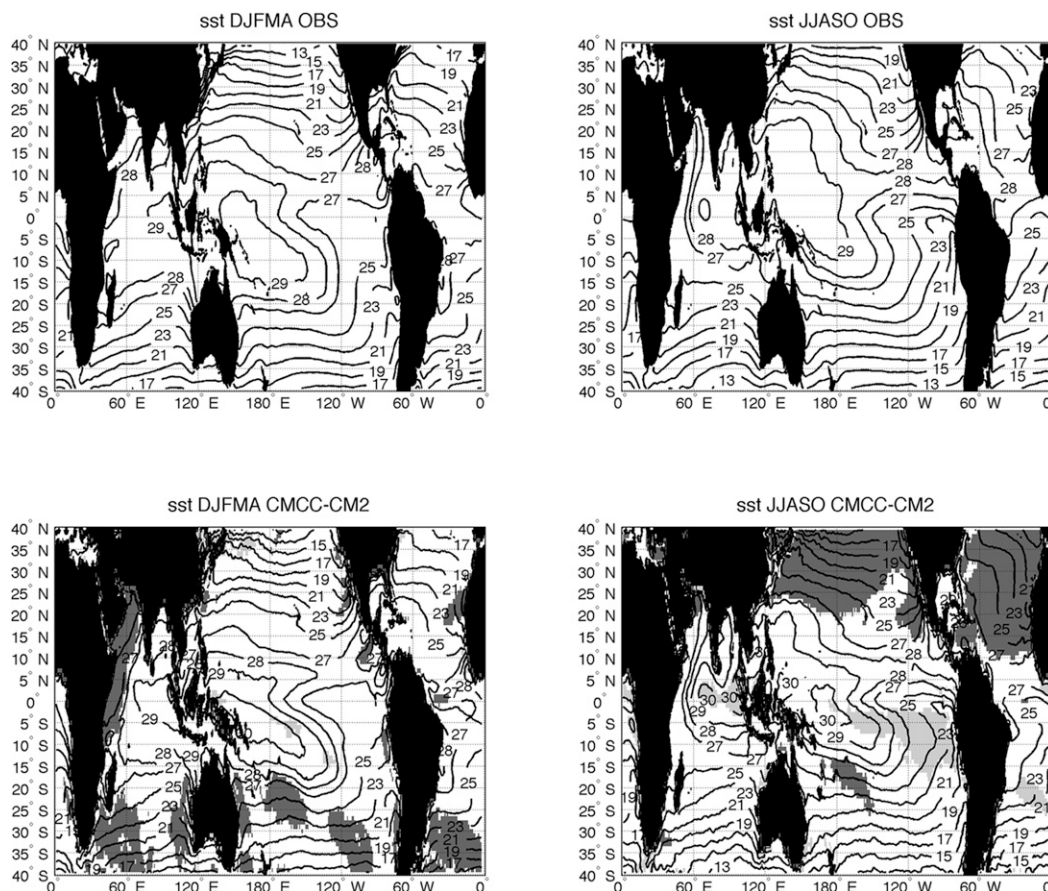
FIG. 1. Seasonal means of SST as obtained from (top) the observations (1981–2000 climatology) and (bottom) the model. (right) The Northern Hemisphere summer mean (JJASO) SST; (left) the extended Southern Hemisphere summer mean (DJFMA) SST. SST contour interval is 2°C from 16° to 26°C and 1°C from 26° to 30°C. Light (dark) gray shaded patterns indicate regions where the SST difference between model and observations is >1°C (<−1°C).

c. Reference data

The following three datasets covering the period 1981–2000 have been used to verify the capability of the model to simulate the observed SST, precipitation rate, and TC activity:

1) for SST, Met Office Hadley Centre Sea Ice and Sea Surface Temperature dataset (HadISST; Rayner et al. 2003);
2) for precipitation rate, Global Precipitation Climatology Project (GPCP) dataset (Bolvin et al. 2009); and
3) for TC activity, National Hurricane Center (NHC) and U.S. Joint Typhoon Warning Center (JTWC) datasets (observed tropical depressions are not considered in the present work).

In the rest of the paper we will refer to these data as observations.

3. Simulation of the tropical climate and TC climatology

a. Mean climate representation in CMCC-CM2-VHR

This section summarizes the main aspects of model mean climate over the two simulated years and compares it with observations, in order to verify how much the modeling environment where simulated TCs develop is similar to the real world. This comparison must be performed keeping in mind that the short simulated period does not allow an extended model bias evaluation. In the observations, the period of maximum TC activity in the Northern Hemisphere (NH) is from June to October (JJASO) and in the Southern Hemisphere (SH) is from December to April (DJFMA). Figure 1 shows the mean DJFMA (left panels) and JJASO (right panels) tropical SST as represented by the model (bottom panels), compared to the observations (top panels). The model comparison with the observations is
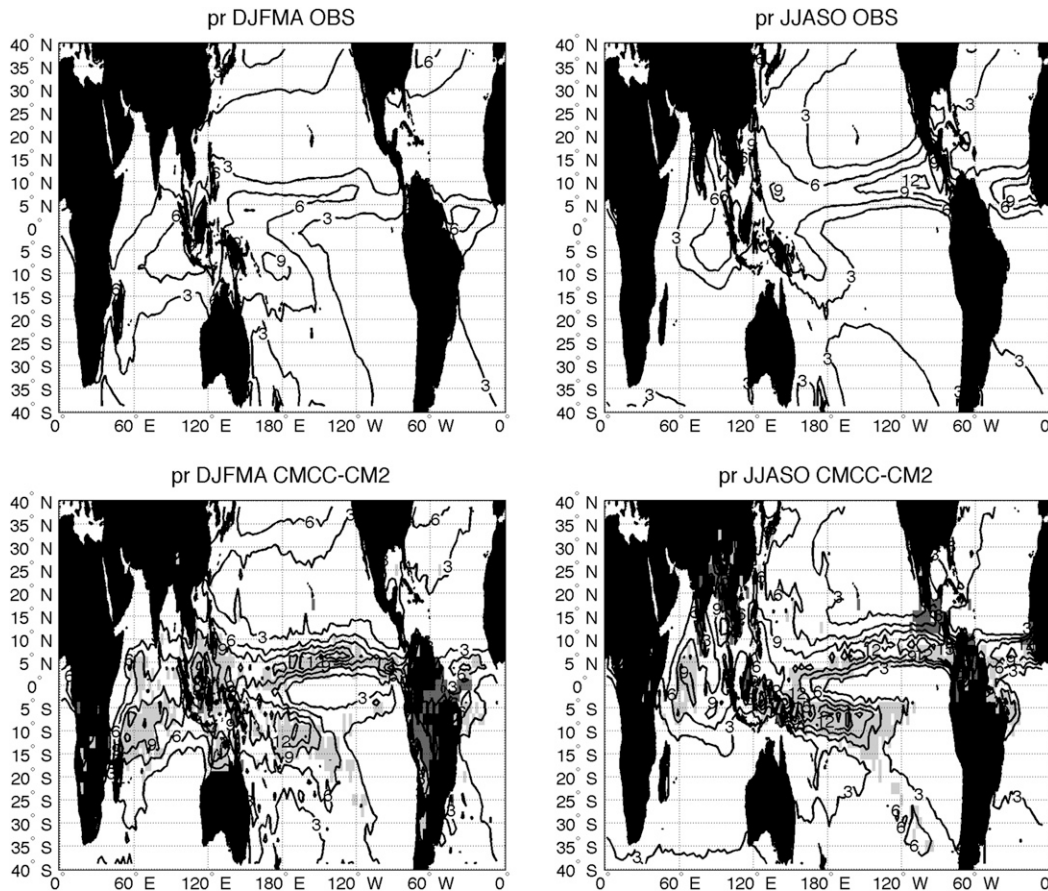
FIG. 2. Seasonal means of total precipitation as obtained from (top) the observations (1981–2000 climatology) and (bottom) the model. (right) The Northern Hemisphere summer mean (JJASO) precipitation; (left) the extended Southern Hemisphere summer mean (DJFMA) precipitation. Precipitation contour interval is 3 mm day^{-1} and range from 3 to 15 mm day^{-1}. Light (dark) gray shaded patterns indicate regions where the difference between model and observations is >3 (<−3) mm day^{-1}.

performed based on the HF simulation only; no significant differences are found between HF and LF simulations in terms of SST, over the TC prone regions during the TC season (not shown). During the JJASO period, there is a pronounced cold bias (between −1° and −2°C) covering the region from 10° to 40°N in the Atlantic and from 25° to 40°N in the western Pacific. In the regions of TC genesis, the modeled temperature bias is generally smaller than 1°C except for the Atlantic.

Figure 2 compares the mean DJFMA (left panels) and JJASO (right panels) modeled precipitation (bottom panels) to the observations (top panels). The model tends to overestimate the precipitation pattern over the tropics, with the tendency to underestimate precipitation pattern only during JJASO over the eastern Pacific. In the Pacific Ocean, the model tends to produce a double ITCZ in both considered seasons. In the Indian Ocean, together with a substantial overestimation during both seasons, there is an evident shift of the rainfall

pattern to the north during the NH extended summer. On the other hand, during the SH extended summer, the modeled rainfall pattern results shifted westward compared to the observations. In the Atlantic Ocean there is a southward shift of the rainfall pattern compared to the observations during JJASO, and the overestimation shown during DJFMA is less pronounced compared to the other basins.

b. TC representation in CMCC-CM2-VHR: Dependencies on the coupling frequency

The ability of the model to simulate TC activity has been assessed comparing model results with observations. The geographical distribution of the TC tracks over the simulated period compared to the observed 1981/82 tracks is shown in Fig. 3. The model reproduces the TC tracks well, except for the South Atlantic area, where the model generates multiple TCs during the considered period, though only one TC has been reported in this region, in March 2004 (Pezza and Simmonds 2005);
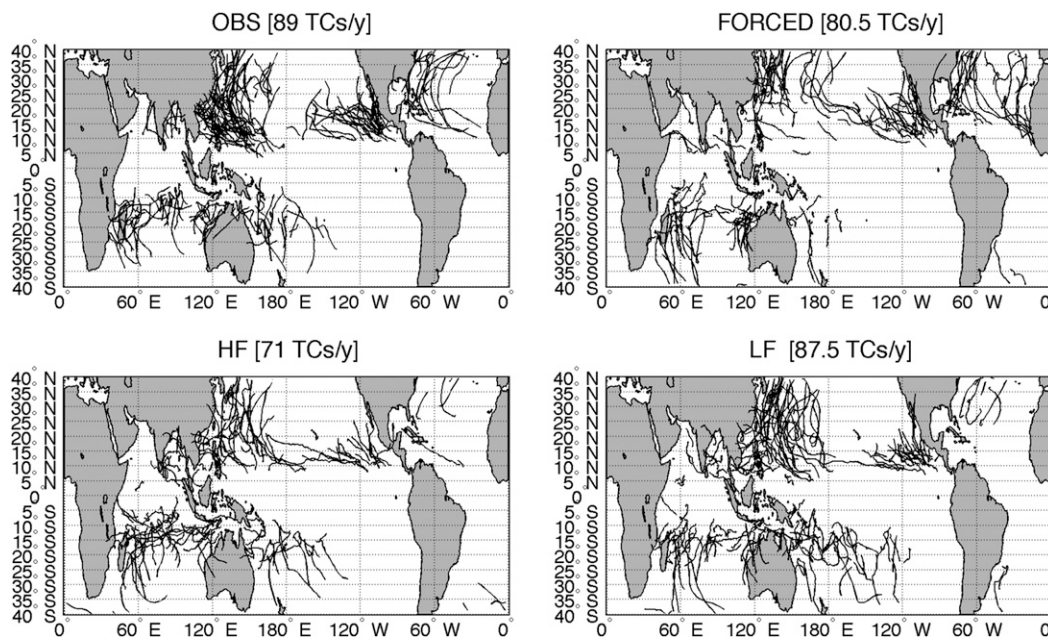
FIG. 3. Tropical cyclone tracks in the 2-yr experiments. Results from (top left) observations, (top right) FORCED experiment, (bottom left) HF experiment, and (bottom right) LF experiment. The observed tracks in (top left) correspond to the 1981/82 period.

this is a common feature of many climate models (Shaevitz et al. 2014), mainly due to SST positive biases over the region. On the other hand, the model tends to represent few TCs in the North Atlantic basin, especially in the coupled configuration (Fig. 3, bottom). Other coupled models show this negative bias, mainly due to the overestimated wind shear over the North Atlantic region, widely recognized to inhibit the development and intensification of TCs (Scoccimarro et al. 2011; Done et al. 2015; Kim et al. 2014). In the coupled simulations, the underestimation of TC count in the Atlantic region (Fig. 3, bottom) could also be explained by the negative SST bias in the coupled simulations (Fig. 1) consistent with Small et al. (2014) and with the more realistic results obtained when the atmospheric model is forced with observed SSTs (Fig. 3, top right).

The global TC count in the two coupled simulations differs by about 20% (71 TCs yr^{-1} in HF compared to 87.5 in LF) with the LF simulation closer to the observations (87.5 compared to the observed long term average of 89 TCs yr^{-1}). The global TC count in the forced simulation (80 TCs yr^{-1}) is in between the results obtained with the coupled runs. These discrepancies can be explained, at least in part, by the interannual variability of the TC count: the standard deviation of the observed TC count over the considered period (1981–2000) is about 10 TCs yr^{-1}. Notably CAM5 (with finite-volume dynamical core configuration) at the same spatial resolution, in forced mode (AMIP 1980–2005), showed a result very similar to the observations, with a standard deviation of about 9 TCs yr^{-1} (Wehner et al. 2014). Unfortunately, we are not able to verify the modeled TC count interannual variability because of the computational effort necessary to extend the simulated period. No significant differences are found in terms of storm duration in the investigated simulations (not shown). Table 1 summarizes the main general statistics on TC activity for each of the simulations.

TABLE 1. General TC statistics in the various CMCC-CM2-VHR simulations.

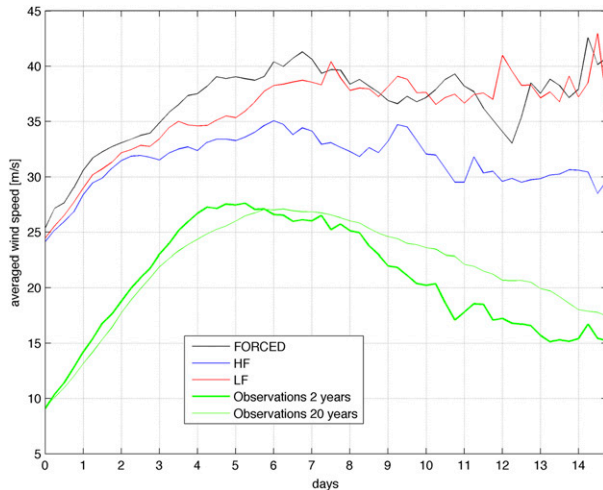|	All TCs (No.)	TC 6-hourly occurrences	Averaged TC duration (days)	No. of					
				Tropical storms	Cat 1	Cat 2	Cat 3	Cat 4	Cat 5
FORCED	161	4382	6.8	46	53	17	27	12	6
LF	175	4688	6.9	55	58	15	28	14	5
HF	142	3916	6.7	52	52	18	15	4	1

FIG. 4. Averaged tropical cyclone wind speed (m s^{-1}) during the first 15 days; 161, 175, 142, and 178 TCs are used to compute the average resulting from FORCED, LF, HF, and observations. The x axis represents the 6-hourly steps from the beginning of the track and it is expressed as days since the beginning of the track.

FIG. 5. Tropical cyclone wind (m s^{-1}) vs minimum SLP (mb) scatterplot. Black, blue, red, and green circles represent FORCED, HF, LF, and observed results, respectively. All the 6-h TC conditions occurring during the 161, 175, 142, and 178 considered TCs are shown. Lines represent quadratic regression fits to the data.

To highlight the TC intensification, Fig. 4 shows the evolution (6-hourly time step sequence within the first 15 days after the TC genesis) of the wind speed as resulting by averaging all modeled TCs in each experiment, compared to the observations. The choice to show only the first 15 days in Fig. 4 is due to the very few TCs surviving more than two weeks. It emerges that the model tends to overestimate TC intensity, especially when the ocean feedback is absent (FORCED simulation), with a smaller error when coupling frequency is high. It is noteworthy that high-frequency coupling leads to a less pronounced intensification (−15%) after the first week and a more marked decay in the second week (Fig. 4) with respect to the low-frequency coupling experiment.

A very similar wind speed at the beginning of the TC development in the HF and LF experiments suggests comparable environmental conditions when TCs start to develop, as confirmed by the very similar SST averaged conditions in the two HF and LF simulations (not shown). The tendency to represent TCs that are too strong, compared to the observations, is a common feature in CAM simulations at the same horizontal resolution (Reed and Jablonowski 2012; Reed et al. 2015). The dependency of this bias on the physics parameterizations is still an open issue.

Figure 5 shows the relationship between maximum surface wind speed (WIND) and minimum sea level pressure (SLP) plotted for every 6 h for detected TCs; the observed WIND–SLP relationship is better represented by the coupled models with no significant differences between the HF and LF experiments. The improvement is substantial when compared to the
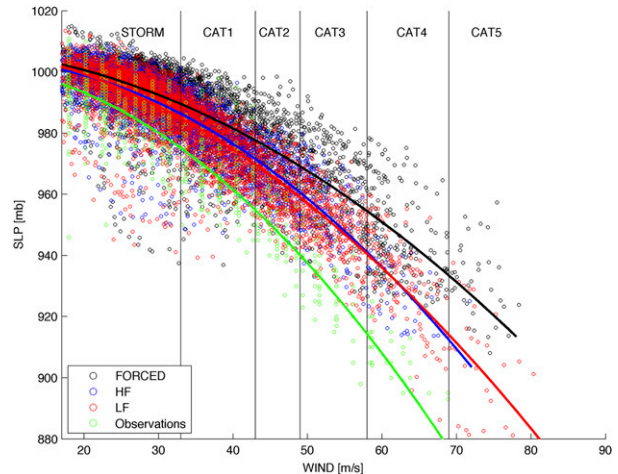
FORCED simulation where SLP associated with supertyphoons (categories 4 and 5) is always above 910 mb (1 mb = 1 hPa). The tropical cyclone WIND–SLP relationship resulting from the CMCC-CM2-VHR simulations is also more realistic than what is found in state-of-the-art atmospheric reanalyses (see Fig. 2 in Murakami 2014). The tendency to a positive bias in TC associated SLP is still present, despite the model ability to represent the most intense TC categories. In a brief comparison with observations, both FORCED and LF simulations produce a higher frequency of larger maximum wind speeds with a wind probability density function skewed toward higher values than observations (Fig. 6).

This is consistent as the atmospheric model, in its ¼° resolution configuration, produces a higher ratio of hurricane strength storms to all TCs per year than observations, as found also in Reed et al. (2015). An additional interesting feature of the distribution of simulated TCs within intensity classes emerges focusing on the left tail of the distribution. Simulated storms (wind speed lower than 33 m s^{-1}) appear to occur more frequently with intensity much higher than observed, indicating that also in this range of intensity the model TCs are characterized by stronger winds. Below 25 m s^{-1} there are many observed storms but few simulated storms (Fig. 6). This suggests that the tendency for a positive bias in the wind intensity associated with TCs appears since the beginning of the modeled TC development, as confirmed by Fig. 4.

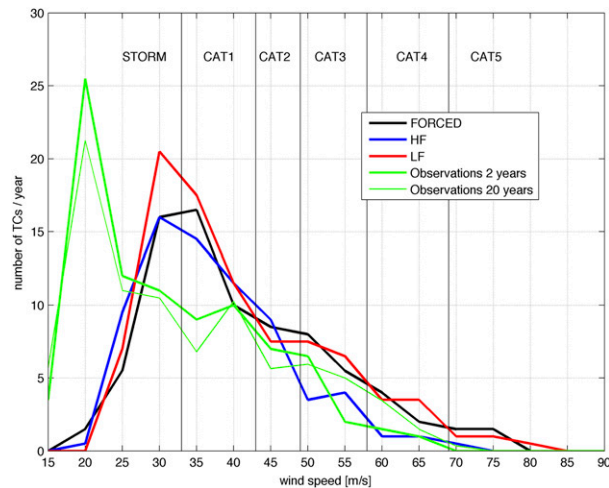The TC count difference found between the LF run and the HF run (Fig. 6, red and blue curves, respectively)

FIG. 6. Annual tropical cyclone count (TCs yr^{-1}) with respect to the associated surface wind speed (m s^{-1}). Black, blue, red, and green lines represent FORCED, HF, LF, and observed results, respectively. Thick green line refers to 1981/82 period (2 yr), and thin green line refers to 1981–2000 period (20 yr). The x axis ranges from 15 to 90 m s^{-1} with 5 m s^{-1} bins. Each x-axis label represents the values between itself and the following one (i.e., the value of 30 on the x axis groups TCs between 30 and 35 m s^{-1}).

is partly responsible for the significant reduction of the power dissipation index (PDI; Emanuel 2005) integrated over the entire period (see Table 2). PDI is a well-recognized indicator of tropical cyclone activity considering both storm frequency and intensity and is of direct interest from the point of view of tropical cyclone contributions to the ocean dynamics (Emanuel 2001). Interestingly, modeled PDI is not significantly influenced by low-frequency coupling (LF run), compared to the FORCED run. On the other hand, regarding coupling atmosphere and ocean at the hourly time scale (HF run), the modeled PDI is better in agreement with observations, reducing the 80% (70%) positive bias in the FORCED (LF) simulation to about 7% in the HF simulation (Table 2). PDI bias in FORCED and LF simulations is mainly due to the overestimation of intense TCs as shown in Fig. 6; the TC counts from cat 3 to cat 5 found in the FORCED and LF experiments are almost halved in the HF simulation (black and red lines compared to blue line) and better in agreement with the observations (green line). To better highlight the differences in TC simulated patterns resulting from a different coupling frequency, Fig. 7 shows composite patterns based on all of the detected TCs in the considered simulations. The less intense TC winds in HF simulation (Fig. 6 and Fig. 7, middle), compared to the LF one, are associated with a more pronounced TC-induced SST anomaly (Fig. 7, top) and to a strong reduction of the TC precipitation amount (Fig. 7, bottom).

TABLE 2. Annual power dissipation index (m^3 s^{-2}) associated with TCs. Top row refers to annual PDI. Bottom row refers to annual PDI normalized by annual TC count.

	Obs	FORCED	LF	HF
PDI ($\times 10^{12}$)	1.52	2.70	2.56	1.63
PDI/(TC No.) ($\times 10^{10}$)	1.36	1.67	1.46	1.14

4. Case study: Cat-5 western Pacific typhoon

To better understand the processes responsible for the weakening of TCs resulting from coupling the atmosphere and the ocean at higher time frequency (HF vs LF results
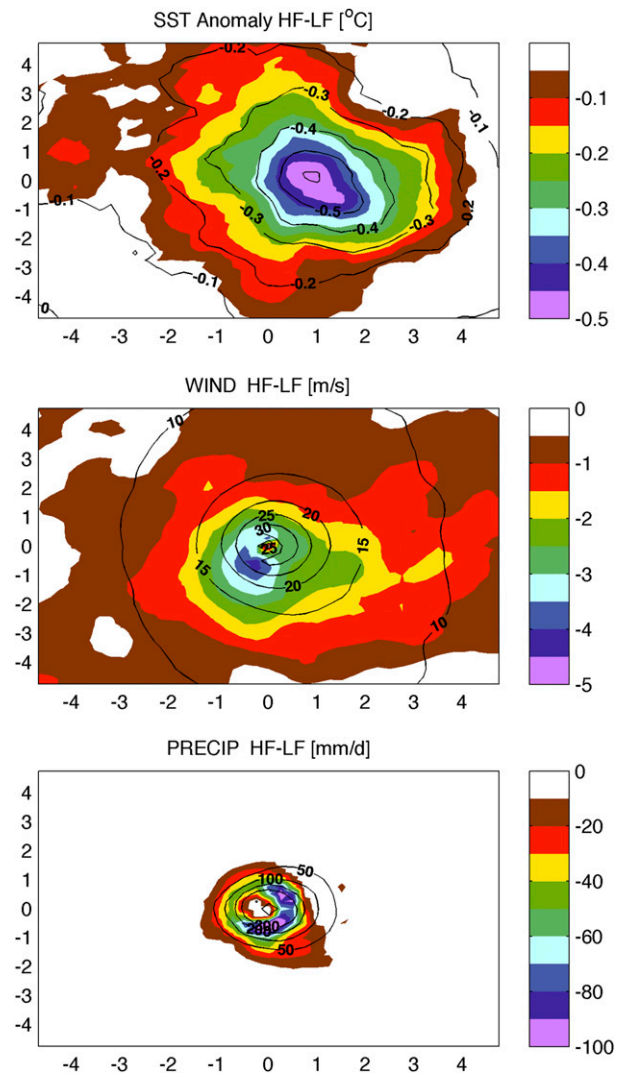

FIG. 7. Composite patterns considering all the TCs in HF simulation (contours) and differences between HF and LF composites (shaded). For each TC, the 6-h step corresponding to the maximum intensity is considered. TC-associated (top) SST anomalies (with respect to 2 days before TC passage; °C), (middle) winds (m s^{-1}), and (bottom) precipitation (mm day^{-1}). The x and y axes correspond to degrees in radius from the TC center.
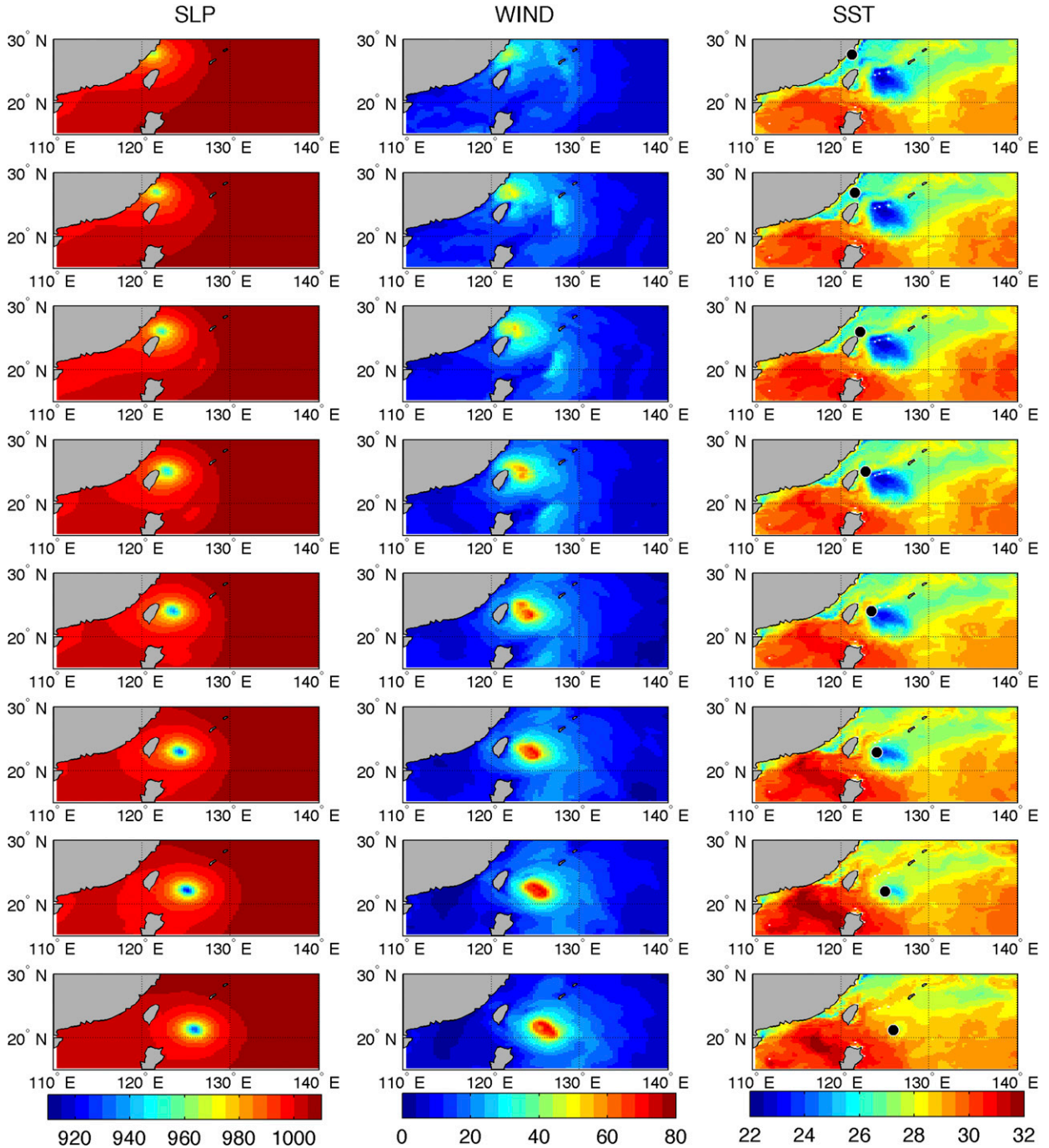
FIG. 8. Time evolution (from bottom to top) of the most intense TC found in the HF simulation. The time step is 6 h, with (bottom) 0000 UTC 1 July, when cat 4 was reached, and (top) 1800 UTC 2 July, when the TC made landfall: (left) SLP (hPa), (center) WIND (m s^{-1}), and (right) SST (°C) fields. Black dots in (right) indicate the TC position [from the minimum SLP in (left)].

described in the section 3b), we focus on the most intense TC (TCJ1), developing in HF simulation: a typhoon reaching cat 5 on 1 July of the second simulated year (J1). To this aim, Fig. 8 shows the time evolution (as 6-hourly frames) of the last two days before landfall of TCJ1 in the

western North Pacific basin. The TCJ1 path, well recognizable following the SLP minimum evolution (Fig. 8, left), is associated with WIND patterns (Fig. 8, center), indicating a wide portion of the basin enveloped by typhoon winds (greater than 33 m s^{-1}), extending from the
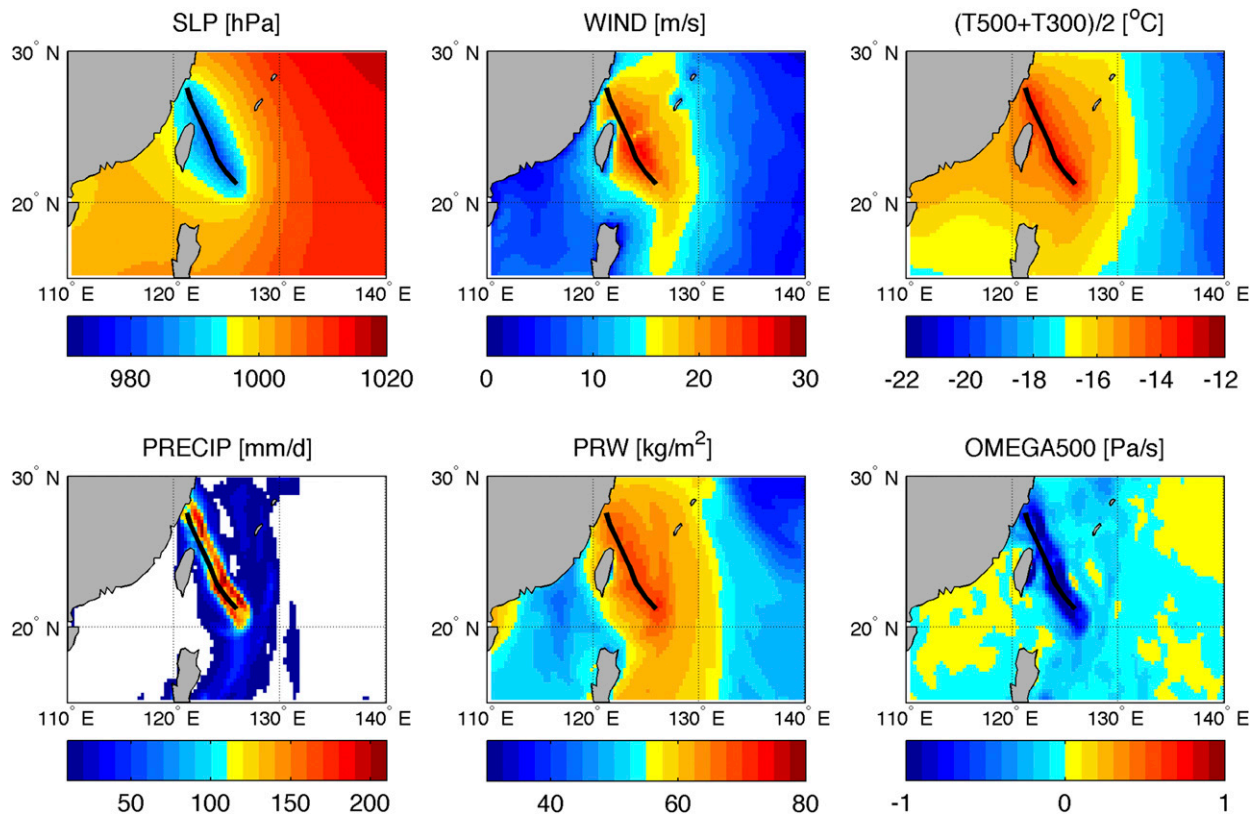
FIG. 9. (top) SLP (hPa), WIND (m s^{-1}), and CORE_TEMP (°C) and (bottom) PRECIP (mm day^{-1}), PRW (kg m^{-2}), and OMEGA500 (Pa s^{-1}) as resulting from a time average over the eight time steps (the 2 days shown in Fig. 7) in the HF simulation. White areas in PRECIP indicates regions where PRECIP is lower than 10 mm day^{-1}. CORE_TEMP is defined as the averaged temperature between 500 and 300 hPa. The black line indicates the TC path (following the minimum SLP in Fig. 7).

TC center to a 300-km-radius region. These strong winds at the surface induce divergence of the water in the first levels of the ocean column and increase the mixing at the base of the mixing layer (not shown). The cold water mixed up from below results in the reduced values of the SST along the TC path. The maximum SST negative anomaly is up to 7°C, leading to 23°C over a region where SST was about 30°C before the TCJ1 passage (Fig. 8, top-right panel vs bottom-right panel). The maximum TC-induced SST anomaly is reached 24–36 h after the TC passage over a certain location (Fig. 8, right, comparing color patterns with black dots indicating the TCJ1 position at a certain time step), consistent with results shown in Scoccimarro et al. (2011) and Lloyd and Vecchi (2011). After landfall (not shown), the TC decays to storm intensity in a few hours.

To have a measure of the averaged characteristics of TCJ1, we computed the time average of several atmospheric (Fig. 9) and ocean (Fig. 10) fields over the two days from maximum TC intensity to landfall (Fig. 8, top and bottom, respectively). An evident warming of the

atmosphere in the TC warm-core sector appears over a wide area (about 10° × 10°) along the TC path (Fig. 9, top right). On the other hand the associated strong precipitation pattern (PRECIP; with maxima up to 200 mm day^{-1} as shown in Fig. 9, bottom left) is confined to an area within a few degrees radius on the right-hand side of the TC center following the TC path, consistent with TC rainfall asymmetry expected in the Northern Hemisphere (Lonfat et al. 2004). This is in agreement with increased deep convection over the same area as made evident in the vertical velocity field at 500 hPa (OMEGA500; Fig. 9, bottom right). Moderate TC-associated precipitation (greater than 10 mm day^{-1}) extends over a wider area, coherently with the huge amount of available precipitable water (PRW) over the region (Fig. 9, bottom center). Focusing on the TC-averaged effect on the ocean side, the SST under the cyclone appears to be about 4°C cooler than in the surrounding region (Fig. 10, top left), with minimum values occurring where the TC reaches the maximum intensity. This TC-induced cooling is responsible for the ''hole'' appearing at the center of the wide positive pattern of
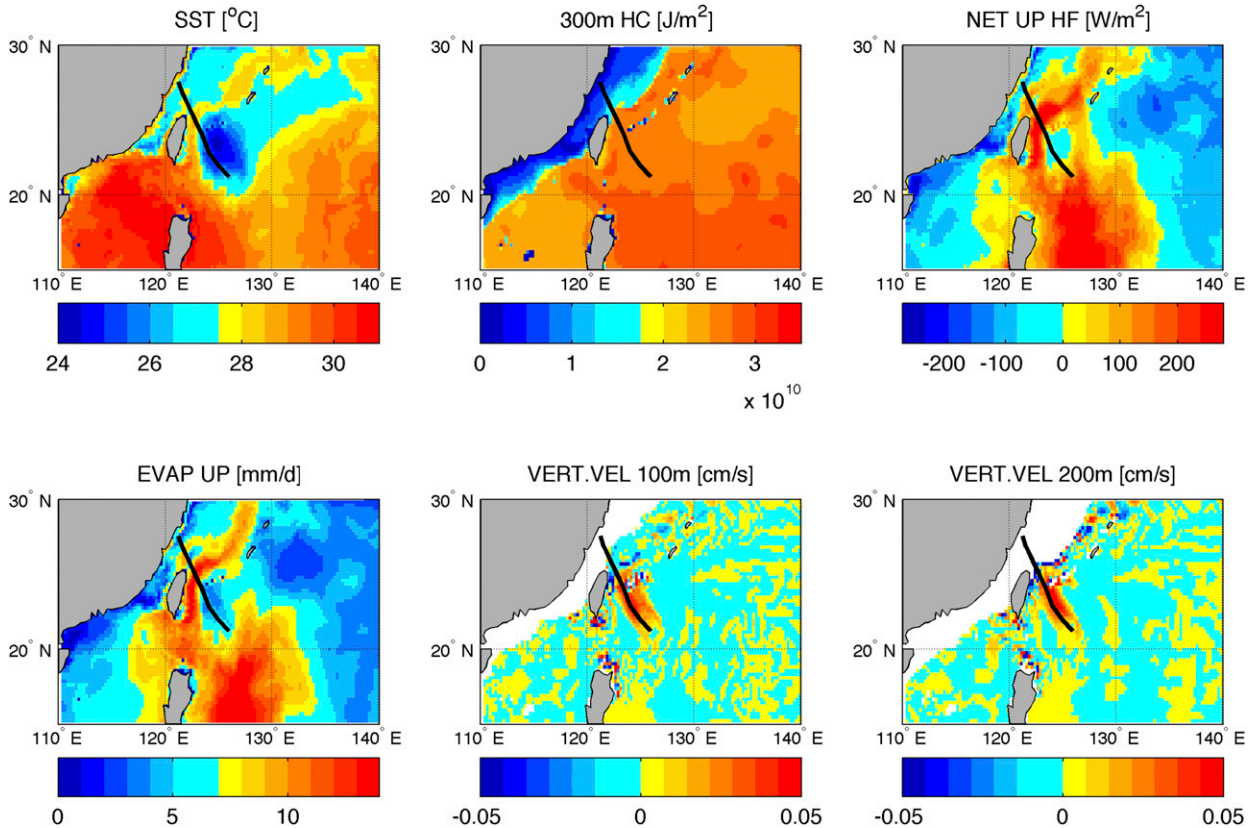
FIG. 10. (top) SST (°C), 300-m heat content (J m^{-2}), and net upward heat flux (W m^{-2}) and (bottom) EVAP (mm day^{-1}) and vertical velocity at 100- and 200-m depth (cm s^{-1}) resulting from a time average over the eight time steps (the 2 days shown in Fig. 7) in the HF simulation. White areas indicate land–sea mask at the considered depth. The black line indicates the TC path (following the minimum SLP in Fig. 7).

the net upward heat flux (Fig. 10, top right) associated with the TC. This is also consistent with the evaporation field (EVAP; Fig. 10, bottom left), indicating the latent heat flux as the major contributor to the net upward heat flux. A measure of the influence of the TC on the ocean is also shown by the vertical velocity at 100- and 200-m depth: an anomalous induced upward vertical velocity on the order of 10^{-2} cm s^{-1} is found at both levels (Fig. 10, bottom center and bottom right).

Starting from the J1 initial condition obtained from the HF simulation, a short simulation (1 month) in LF configuration (coupling at the daily time frequency) has been then performed to have a direct measure of the high-frequency coupling effect on the investigated TCJ1. Figure 11 highlights the emerging differences (HF minus LF) in TCJ1 during the same eight 6-hourly frames (2 days) shown in Fig. 8. The choice of a 2-day time window is due to the TC landfall after 48 h. In addition, after one day, the TCJ1 trajectories represented in the two different HF and LF configurations start to diverge (see black and red dots in Fig. 11, right), inhibiting the possibility to compare results in terms of Eulerian averages. The first 6-hourly frame,

corresponding to the 6-hourly results after J1 initial conditions (Fig. 11, bottom), does not show significant differences, and a weakening of TCJ1 intensity in HF configuration starts to emerge after 12 h. The reduced intensity in HF is evident both in terms of sea level pressure and 10-m wind speed (Fig. 11, left and center, respectively) and appears immediately after the emerged negative signal in the sea surface temperature (Fig. 11, bottom right). The more pronounced cooling of the surface in the HF simulation (up to −5°C), because of the better representation of the TC dynamical effect on the ocean, covers a wide area along the TCJ1 path and peaks one day after the maximum TC intensity was reached (J1 plus 1 day). Interestingly, associated with the negative values in SST difference between HF and LF, a positive pattern appears (Fig. 11, top right) over the region where TCJ1 transited one day before. This is the effect of "false" TC-induced pumping in the ocean in the LF configuration, resulting from the longer delay in updating atmospheric surface forcing sent to the ocean model, compared to the HF setup (24 vs 1.5 h).

A measure of the different representation of TCJ1 in the two configurations is shown in Fig. 12. The HF − LF

SLP   WIND   SST
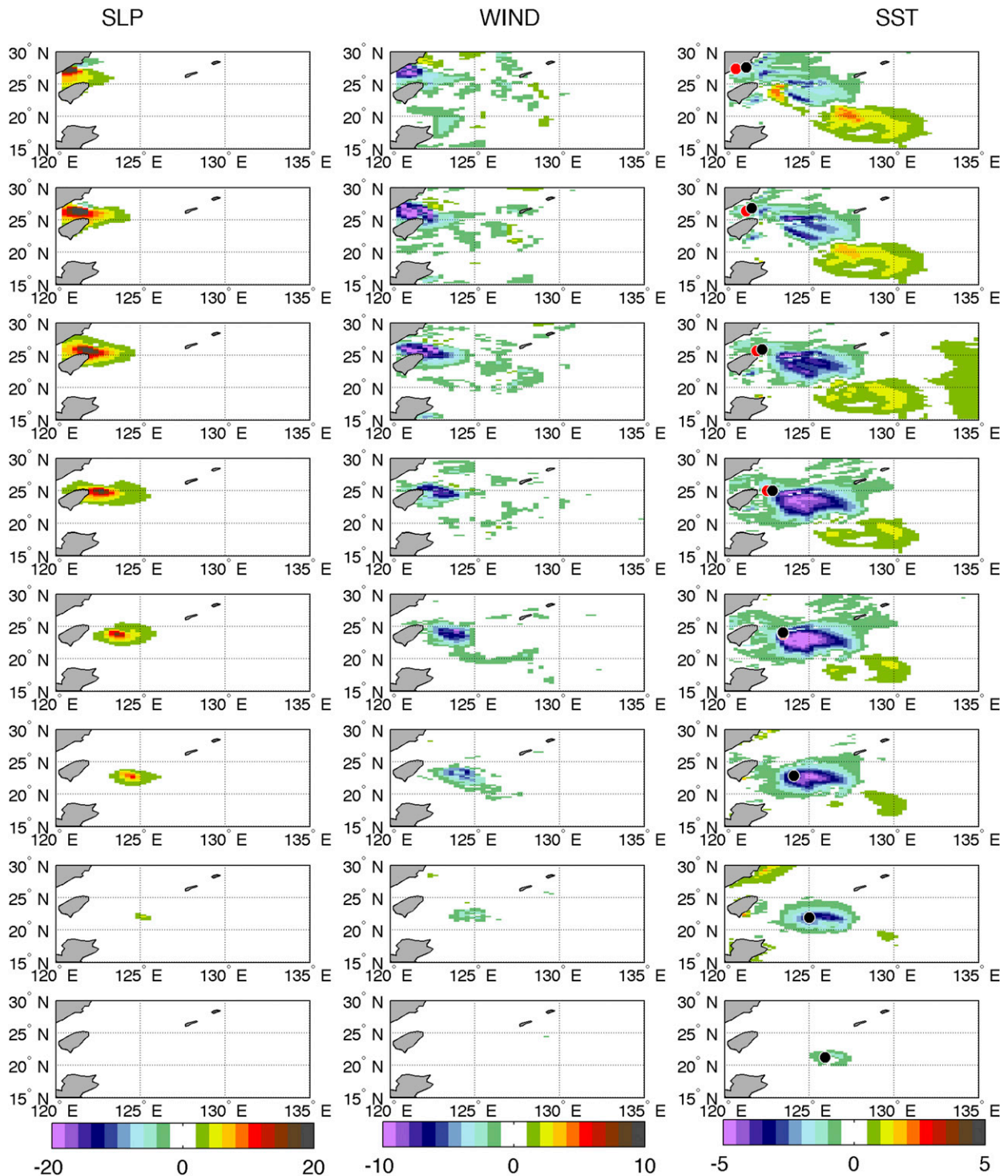

FIG. 11. Time evolution (from bottom to top) of the most intense TC found in HF simulation in terms of differences between the HF and LF simulations (HF − LF). The time step is 6 h, with (bottom) 0000 UTC 1 July, when cat 4 was reached and (top) 1800 UTC 2 July, when the TC made landfall. Differences in (left) SLP (hPa), (center) WIND (m s^{-1}), and (right) SST (°C) fields. Black and red dots in (right) indicate the TC position in HF and LF configuration, respectively. Notably, red and black dots overlap at least in the first six time steps.
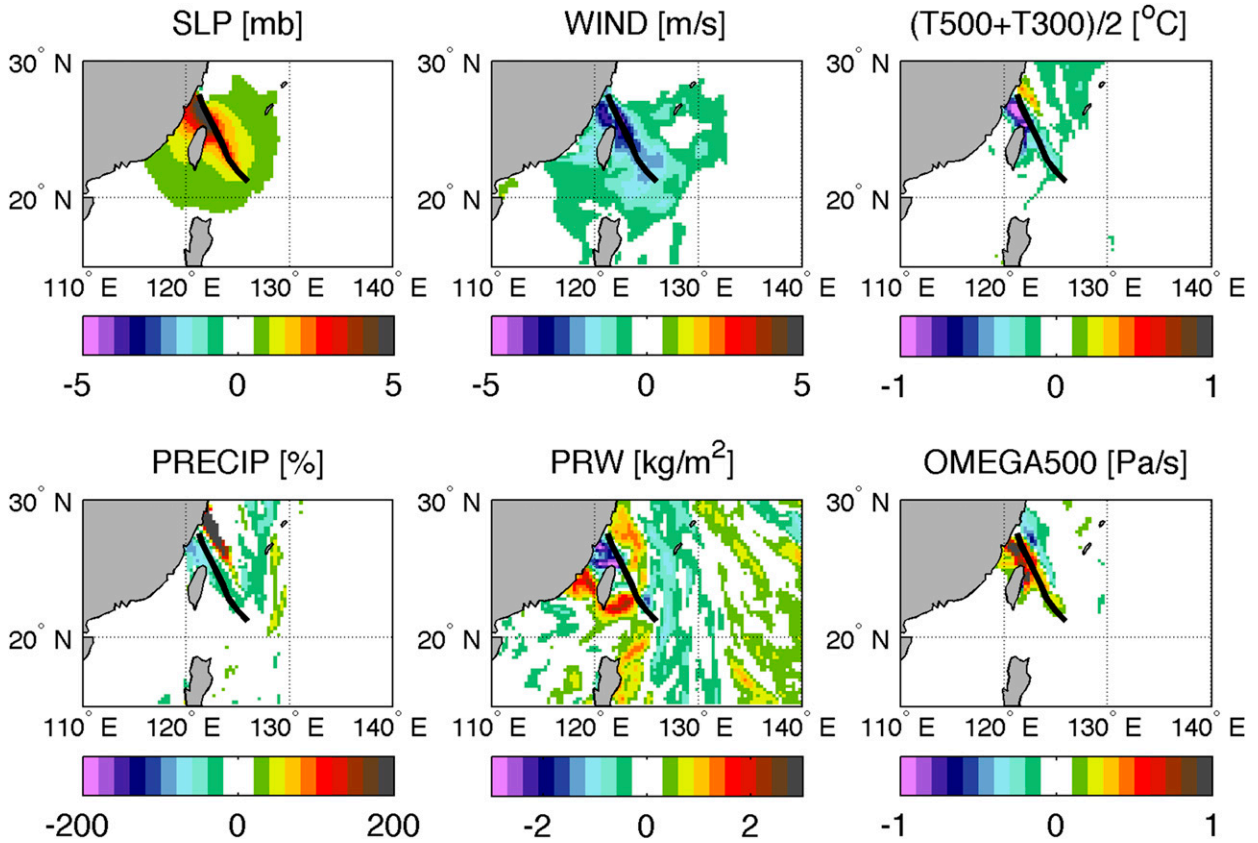
FIG. 12. Differences between the HF and LF simulations (HF − LF) in (top) SLP (hPa), WIND (m s^{-1}), and CORE_TEMP (°C) and (bottom) PRECIP (%), PRW (kg m^{-2}), and OMEGA500 (Pa s^{-1}) as a time average over the eight time steps (as in Fig. 10). The black line indicates the TC path (following the minimum SLP in Fig. 7).

differences in sea level pressure and 10-m wind speed are also associated with changes in the magnitude of the typhoon warm core on the order of 1°C. Once approaching landfall, coherent with the trajectories' divergence already mentioned (Fig. 11), a dipole in the warm-core difference pattern appears (Fig. 12, top right) as confirmed in precipitation (PRECIP; Fig. 12, bottom left) and OMEGA500 (Fig. 12, bottom right). This suggests that, together with small changes in the TCJ1 path in the two considered experiments defined based on SLP, a different TC tilting plays a role in defining the vertical structure of the system: the dipole in the differences computed for high-level patterns is more pronounced than what is found at the surface. A less clear pattern is associated with the differences in the vertically integrated water content (PRW), despite a coherent dipole structure close to the coastal region (Fig. 12, bottom center). On the ocean side the already highlighted false TC-induced effect, because of the delayed communication between atmospheric and ocean components in the LF setup, appears also when averaging over the two considered days (Fig. 13, top left). This is

confirmed by differences in the heat content (HC) of the upper 300 m (Fig. 13, top center) showing up to 5% negative values along the TCJ1 track and positive values of the same magnitude along the TC path prior to J1. Associated with the HF − LF difference in SST, a remarkable negative pattern in the net upward heat flux also appears (Fig. 13, top right). In particular over a wide region (about 200-km radius) following the TC path, differences up to −400 W m^{-2} are found, leading to a huge decrease of the heat released to the atmosphere in HF compared to LF and thus to a reduced fueling of the TC when coupling ocean and atmosphere at the higher frequency. The relative role played by the latent heat flux in this process is highlighted by the differences emerging in the evaporation field (Fig. 13, bottom left).

To verify and quantify the role of the coupling frequency in determining TC-induced changes in the vertical structure of the ocean, we focused on a section defined following the TC path (black lines in Figs. 9, 10, 12, and 13) both in terms of ocean temperature and vertical velocity (Fig. 14). The more pronounced TC-induced cooling effect (Fig. 13) in the HF simulation
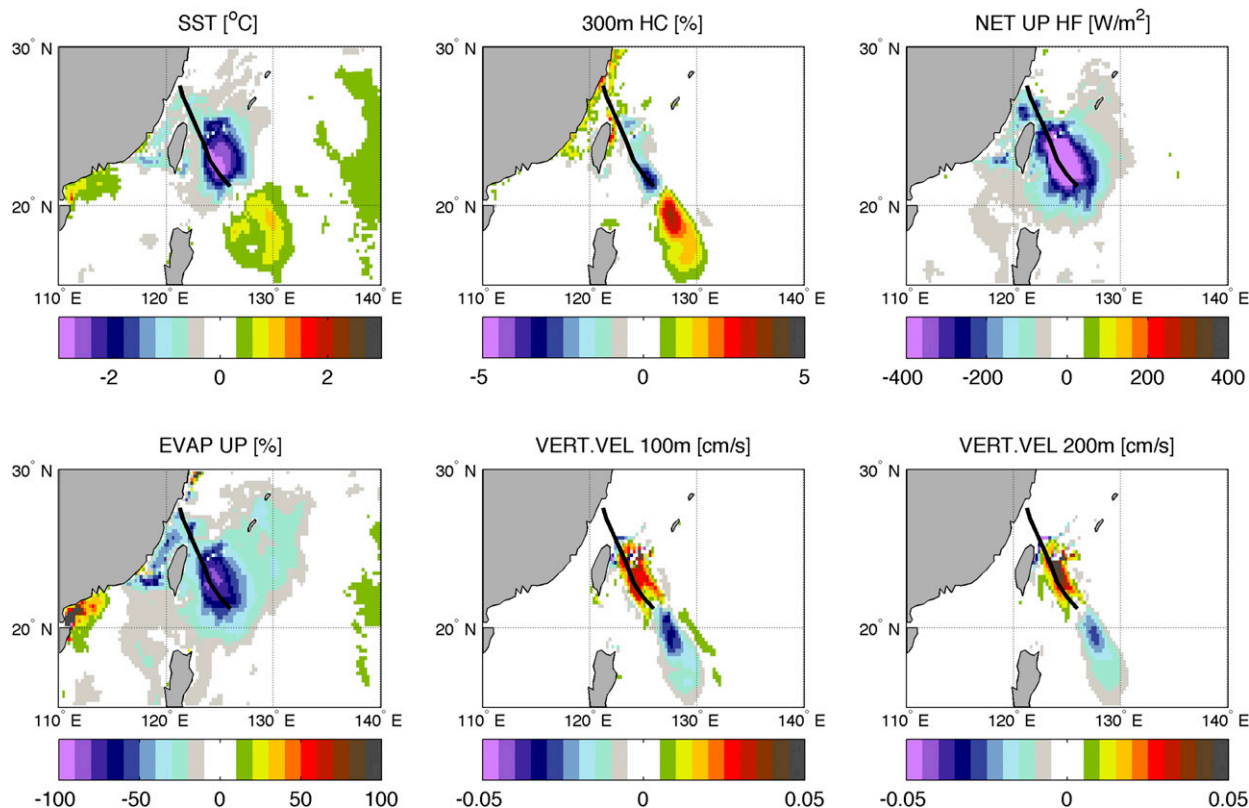
FIG. 13. Differences between the HF and LF simulations (HF − LF) in (top) SST (°C), 300-m HC (%), and net upward heat flux (W m^{-2}) and (bottom) EVAP (%) and vertical velocity at 100- and 200-m depth (cm s^{-1}) as a time average over the eight time steps (the 2 days shown in Fig. 7). The black line indicates the TC path (following the minimum SLP in Fig. 7).

affects the upper 30 m and is associated with a warm pattern between 30 and 70 m (Fig. 14, left). The more efficient mixing of the upper ocean induced by TCs (Leipper 1967; Price 1981) in the HF simulation is also evident from the vertical profiles of temperature within the upper 100 m. The two profiles (relative to the HF and LF simulations) reflect the theoretical expected TC-induced mixing (Emanuel 2001). In addition, a more pronounced cooling of the deep ocean (below 100 m) in the HF experiment appears (Fig. 15, left) coherently with a significant increase of the ocean vertical velocity along the TC track (Fig. 14 and Fig. 15, right), providing cold water from the deep ocean to the intermediate layers. It is noteworthy that the most intense TC-induced vertical velocity, made evident in the HF experiment, is found between 1000- and 2000-m depth (Fig. 14, right).

5. Discussion and conclusions

The ocean is the major source of energy for tropical cyclones. Thus, understanding the interplay between TCs and the ocean is crucial to clarify the ocean role in TC development and intensification. In this work we report on the role of short-term (order of hours) atmosphere–ocean interaction in modulating the TC intensity during its evolution. This is made possible thanks to the new generation of a fully coupled model developed at CMCC ($\frac{1}{4}$° in both atmosphere and ocean components) able to represent the most intense observed TC categories. A first assessment to verify systematic differences in TC intensity and count has been done comparing the results from a 2-yr-long simulation forced by prescribed SSTs (FORCED experiment) to results obtained from two 2-yr-long simulations with the fully coupled model, where the ocean is coupled at two different time frequencies: daily and hourly (LF and HF, respectively).

We found 4382, 4688, and 3916 TC conditions every 6 h, corresponding to 161, 175, and 142 unique TCs in the FORCED, LF, and HF 2-yr experiments, respectively. The lack of weak storms found in the model (Fig. 4) is not dependent on the coupling frequency, suggesting that its origin is intrinsic to the atmospheric model. While this is an interesting issue to address, it is outside of the scope of the present work.

The differences found in TC count in the different experiments are more or less of the same magnitude of
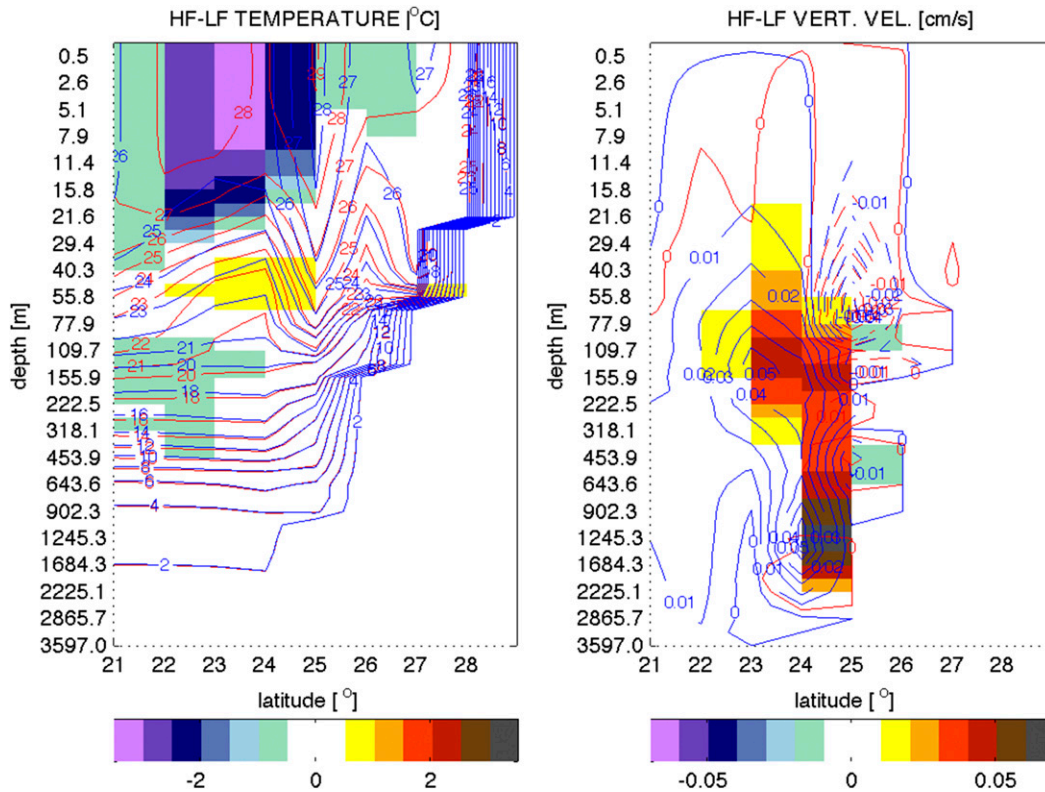
FIG. 14. Differences between HF and LF simulation (HF − LF) along the ocean section following the TC path. The path is defined following 6-hourly SLP minimum shown in Fig. 7. The differences (patterns) are computed based on the 2-day-averaged fields (as in Fig. 13). (left) Temperature differences (°C) and (right) differences in vertical velocity (cm s^{-1}). Contour lines represent HF (blue) and LF (red) values used to compute the shown differences (patterns).

the observed interannual variability, but for an evaluation of TC count modulation due to the different representation of the interaction with the ocean, longer simulations are needed. On the other hand, a more realistic representation of the high-frequency surface feedback strongly affects the average TC intensity. This is clear from evaluating the power dissipation index at the global scale. PDI is better in agreement with observations when coupling at the higher frequency, reducing by one order of magnitude the positive bias (from 70% to 7%) shown in the forced and low-frequency experiments. This result suggests that the high-frequency feedback with the ocean strongly affects TC activity in terms of storm intensity, answering the scientific question we posed, especially regarding very intense TCs. A reduction of intense TC count (Fig. 6), coupling at the higher frequency, is also reflected in the reduction of the integrated PDI (Table 2) since PDI magnitude is mainly driven by intense TCs (i.e., PDI follows the cube of the wind speed).

To better highlight the processes involved in determining the aforementioned effect, we focused on a case study. The most intense category-5 typhoon found in the HF simulation has been simulated two times, rerunning the coupled model with daily and hourly coupling frequency (LF and HF configuration, respectively) starting from the same initial condition, defined based on the timing of the TC maximum intensity. The better representation of the SST feedback in the HF simulation (Fig. 11), made evident after 12 h, reduces by more than 20% the TC intensity in the following 36 h, before landfall. This is also evident in terms of a less intense TC warm core, reduced vertical velocity at 500 hPa, and less pronounced SLP minimum (Fig. 12) in HF compared to LF. The case study findings are consistent with the PDI statistics resulting from the whole simulation, reinforcing the evidence that TC self-induced cooling plays a role in controlling TC intensification.

We found that high horizontal resolutions (order of ¼° in both atmosphere and ocean models) make the representation of fast-moving and intense events very sensitive to the coupling frequency. The low-frequency coupling (LF simulation) tends to reduce the cooling effect on the TC itself since the system had already
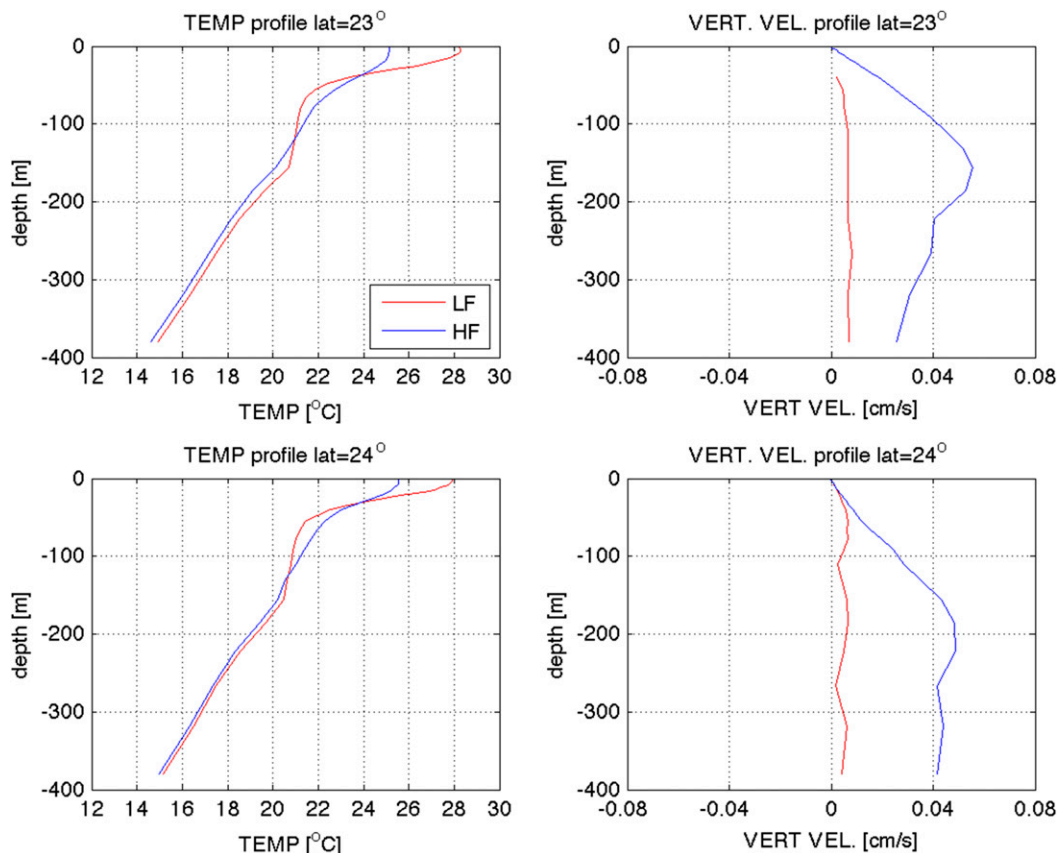
FIG. 15. HF and LF profiles for (left) ocean temperature (°C) and (right) vertical velocity (cm s^{-1}) corresponding to the TC position (top) 12 and (bottom) 18 h after J1. The profiles are taken from a 2-day time average, as in Fig. 14. Profiles in (top) and (bottom) correspond to the position along the TC path, located at about 23° and 24°N, respectively.

moved on when the effect of the cooler SST was brought back to the atmosphere. In addition to the effect on the TC intensity due to a more pronounced surface cooling representation at the high frequency (Fig. 11), the coupling time resolution also affects the magnitude and the location of the TC fingerprint on the ocean subsurface. In terms of magnitude, focusing on a cat-5 typhoon, the cooling, warming, and cooling effect induced by the TC on the surface, subsurface, and deep ocean, respectively, is more evident when coupling at the high frequency (Fig. 15), with a difference in the TC-induced maximum surface cooling on the order of 7°C on the 6-hourly averages (Fig. 11). This is mainly due to the less intense wind stresses, causing water divergence at the surface, when coupling at the daily frequency (LF simulation); wind stresses are computed based on winds accumulated over the coupling period, as with the other fluxes into the ocean. Moreover, the low-frequency (daily) coupling causes the persistence of false TC pumping effect over regions where the TC is not present anymore. This spurious effect is partially

filtered out in low-resolution models but appears to be not negligible (Fig. 13) once the horizontal resolution is sufficiently high to make the alignment of the TC location on the atmospheric and ocean grids more difficult to achieve when coupling at the daily frequency.

This work suggests that the new generation of fully coupled general circulation models are promising tools to investigate the climate change effects on TCs and the climate control role for TCs. The model involved in this study is participating in the High Resolution Model Intercomparison Project (HighResMIP; Haarsma et al. 2016; http://www.wcrp-climate.org/index.php/modelling-wgcm-mip-catalogue/429-wgcm-hiresmip) developed in the context of the World Climate Research Programme. The great effort in increasing the horizontal resolution of climate models within HighResMIP will give an unprecedented boost to the TC–climate interaction studies, provided that a high coupling frequency between the ocean and the atmospheric components is applied.

Previous work suggests that TCs can affect the deep ocean in terms of induced anomalies in the vertical

velocity (Scoccimarro et al. 2011). This is confirmed by the present study, where the TC effect on the deep ocean, highlighted by the high-coupling-frequency experiment compared to the low-frequency one, is found down to 1000 m (Fig. 14). A more detailed investigation of the processes driving this effect is left for future work.

REFERENCES

Bacmeister, J. T., M. F. Wehner, R. B. Neale, A. Gettelman, C. Hannay, P. H. Lauritzen, J. M. Caron, and J. E. Truesdale, 2014: Exploratory high-resolution climate simulations using the Community Atmosphere Model (CAM). *J. Climate*, **27**, 3073–3099, doi:10.1175/JCLI-D-13-00387.1.

——, K. A. Reed, C. Hannay, P. Lawrence, S. Bates, J. E. Truesdale, N. Rosenbloom, and M. Levy, 2016: Projected changes in tropical cyclone activity under future warming scenarios using a high-resolution climate model. *Climatic Change*, doi:10.1007/s10584-016-1750-x, in press.

Bell, R., J. Strachan, P. L. Vidale, K. Hodges, and M. Roberts, 2013: Response of tropical cyclones to idealized climate change experiments in a global high-resolution coupled general circulation model. *J. Climate*, **26**, 7966–7980, doi:10.1175/JCLI-D-12-00749.1.

Bolvin, D. T., R. F. Adler, G. J. Huffman, E. J. Nelkin, and J. P. Poutiainen, 2009: Comparison of GPCP monthly and daily precipitation estimates with high-latitude gauge observations. *J. Appl. Meteor. Climatol.*, **48**, 1843–1857, doi:10.1175/2009JAMC2147.1.

Bueti, M. R., I. Ginis, L. M. Rothstein, and S. M. Griffies, 2014: Tropical cyclone–induced thermocline warming and its regional and global impacts. *J. Climate*, **27**, 6978–6999, doi:10.1175/JCLI-D-14-00152.1.

Camargo, S. J., 2013: Global and regional aspects of tropical cyclone activity in the CMIP5 models. *J. Climate*, **26**, 9880–9902, doi:10.1175/JCLI-D-12-00549.1.

Craig, A. P., M. Vertenstein, and R. Jacob, 2012: A new flexible coupler for earth system modeling developed for CCSM4 and CESM1. *Int. J. High Perform. Comput. Appl.*, **26**, 31–42, doi:10.1177/1094342011428141.

Daloz, A. S., F. Chauvin, and F. Roux, 2012: Impact of the configuration of stretching and ocean–atmosphere coupling on tropical cyclone activity in the variable-resolution GCM ARPEGE. *Climate Dyn.*, **39**, 2343–2359, doi:10.1007/s00382-012-1561-3.

Done, J. M., G. J. Holland, C. L. Bruyère, L. R. Leung, and A. Suzuki-Parker, 2015: Modeling high-impact weather and climate: Lessons from a tropical cyclone perspective. *Climatic Change*, **129**, 381–395, doi:10.1007/s10584-013-0954-6.

Emanuel, K., 2001: Contribution of tropical cyclones to meridional heat transport by the oceans. *J. Geophys. Res.*, **106**, 14 771–14 781, doi:10.1029/2000JD900641.

——, 2005: Increasing destructiveness of tropical cyclones over the past 30 years. *Nature*, **436**, 686–688, doi:10.1038/nature03906.

——, 2015: Effect of upper-ocean evolution on projected trends in tropical cyclone activity. *J. Climate*, **28**, 8165–8170, doi:10.1175/JCLI-D-15-0401.1.

——, C. DesAutels, C. Holloway, and R. Korty, 2004: Environmental control of tropical cyclone intensity. *J. Atmos. Sci.*, **61**, 843–858, doi:10.1175/1520-0469(2004)061<0843:ECOTCI>2.0.CO;2.

Fogli, P. G., and D. Iovino, 2014: CMCC–CESM–NEMO: Toward the new CMCC Earth System Model. CMCC Research Rep. RP0248, 19 pp. [Available online at http://www.cmcc.it/wp-content/uploads/2015/02/rp0248-ans-12-2014.pdf.]

Haarsma, R. J., and Coauthors, 2016: High Resolution Model Intercomparison Project (HighResMIP v1.0) for CMIP6. *Geosci. Model Dev.*, **9**, 4185–4208, doi:10.5194/gmd-9-4185-2016.

Horn, M., and Coauthors, 2014: Tracking scheme dependence of simulated tropical cyclone response to idealized climate simulations. *J. Climate*, **27**, 9197–9213, doi:10.1175/JCLI-D-14-00200.1.

Huang, P., I.-I. Lin, C. Chou, and R.-H. Huang, 2015: Change in ocean subsurface environment to suppress tropical cyclone intensification under global warming. *Nat. Commun.*, **6**, 7188, doi:10.1038/ncomms8188.

Hunke, E., and W. H. Lipscomb, 2008: CICE: The Los Alamos sea ice model, documentation and software, version 4.0. Los Alamos National Laboratory Tech. Rep. LA-CC-06-012, 76 pp.

Hurrell, J. W., and Coauthors, 2013: The Community Earth System Model: A framework for collaborative research. *Bull. Amer. Meteor. Soc.*, **94**, 1339–1360, doi:10.1175/BAMS-D-12-00121.1.

Kim, H.-S., G. A. Vecchi, T. R. Knutson, W. G. Anderson, T. L. Delworth, A. Rosati, F. Zeng, and M. Zhao, 2014: Tropical cyclone simulation and response to CO_2 doubling in the GFDL CM2.5 high-resolution coupled climate model. *J. Climate*, **27**, 8034–8054, doi:10.1175/JCLI-D-13-00475.1.

Lawrence, D. M., and Coauthors, 2011: Parameterization improvements and functional and structural advances in version 4 of the Community Land Model. *J. Adv. Model. Earth Syst.*, **3**, M03001, doi:10.1029/2011MS000045.

Leipper, D. F., 1967: Observed ocean conditions and Hurricane Hilda, 1964. *J. Atmos. Sci.*, **24**, 182–196, doi:10.1175/1520-0469(1967)024<0182:OOCAHH>2.0.CO;2.

Lloyd, I. D., and G. A. Vecchi, 2011: Observational evidence for oceanic controls on hurricane intensity. *J. Climate*, **24**, 1138–1153, doi:10.1175/2010JCLI3763.1.

Lonfat, M., F. D. Marks, and S. S. Chen, 2004: Precipitation distribution in tropical cyclones using the Tropical Rainfall Measuring Mission (TRMM) Microwave Imager: A global perspective. *Mon. Wea. Rev.*, **132**, 1645–1660, doi:10.1175/1520-0493(2004)132<1645:PDITCU>2.0.CO;2.

Madec, G., and Coauthors, 2008: NEMO ocean engine version 3.0. Institut Pierre-Simon Laplace Rep. 27, 209 pp. [Available online at http://www.nemo-ocean.eu/Media/Files/NEMO_book_V3_0.pdf.]

Murakami, H., 2014: Tropical cyclones in reanalysis data sets. *Geophys. Res. Lett.*, **41**, 2133–2141, doi:10.1002/2014GL059519.

——, and Coauthors, 2015: Simulation and prediction of category 4 and 5 hurricanes in the high-resolution GFDL HiFLOR coupled climate model. *J. Climate*, **28**, 9058–9079, doi:10.1175/JCLI-D-15-0216.1.

Oleson, K. W., and Coauthors, 2010: Technical description of version 4.0 of the Community Land Model (CLM). NCAR Tech. Note NCAR/TN-478+STR, 257 pp., doi:10.5065/D6FB50WZ.

Pezza, A. B., and I. Simmonds, 2005: The first South Atlantic hurricane: Unprecedented blocking, low shear and climate change. *Geophys. Res. Lett.*, **32**, L15712, doi:10.1029/2005GL023390.

Price, J. F., 1981: Upper ocean response to a hurricane. *J. Phys. Oceanogr.*, **11**, 153–175, doi:10.1175/1520-0485(1981)011<0153:UORTAH>2.0.CO;2.

Rayner, N. A., D. E. Parker, E. B. Horton, C. K. Folland, L. V. Alexander, D. P. Rowell, E. C. Kent, and A. Kaplan, 2003: Global analyses of sea surface temperature, sea ice, and night

marine air temperature since the late nineteenth century. *J. Geophys. Res.*, **108**, 4407, doi:10.1029/2002JD002670.

Reed, K. A., and C. Jablonowski, 2012: Idealized tropical cyclone simulations of intermediate complexity: A test case for AGCMs. *J. Adv. Model. Earth Syst.*, **4**, M04001, doi:10.1029/2011MS000099.

——, J. T. Bacmeister, N. A. Rosenbloom, M. F. Wehner, S. C. Bates, P. H. Lauritzen, J. E. Truesdale, and C. Hannay, 2015: Impact of the dynamical core on the direct simulation of tropical cyclones in a high-resolution global model. *Geophys. Res. Lett.*, **42**, 3603–3608, doi:10.1002/2015GL063974.

Scoccimarro, E., and Coauthors, 2011: Effects of tropical cyclones on ocean heat transport in a high-resolution coupled general circulation model. *J. Climate*, **24**, 4368–4384, doi:10.1175/2011JCLI4104.1.

——, S. Gualdi, G. Villarini, G. A. Vecchi, M. Zhao, K. Walsh, and A. Navarra, 2014: Intense precipitation events associated with landfalling tropical cyclones in response to a warmer climate and increased CO_2. *J. Climate*, **27**, 4642–4654, doi:10.1175/JCLI-D-14-00065.1.

Shaevitz, D. A., and Coauthors, 2014: Characteristics of tropical cyclones in high-resolution models in the present climate. *J. Adv. Model. Earth Syst.*, **6**, 1154–1172, doi:10.1002/2014MS000372.

Small, R. J., and Coauthors, 2014: A new synoptic scale resolving global climate simulation using the Community Earth System Model. *J. Adv. Model. Earth Syst.*, **6**, 1065–1094, doi:10.1002/2014MS000363.

Sriver, R. L., M. Goes, M. E. Mann, and K. Keller, 2010: Climate response to tropical cyclone-induced ocean mixing in an Earth system model of intermediate complexity. *J. Geophys. Res.*, **115**, C10042, doi:10.1029/2010JC006106.

Villarini, G., D. A. Lavers, E. Scoccimarro, M. Zhao, M. F. Wehner, G. Vecchi, and T. Knutson, 2014: Sensitivity of tropical cyclone rainfall to idealized global-scale forcings. *J. Climate*, **27**, 4622–4641, doi:10.1175/JCLI-D-13-00780.1.

Vincent, E. M., K. A. Emanuel, M. Lengaigne, J. Vialard, and G. Madec, 2014: Influence of upper ocean stratification interannual variability on tropical cyclones. *J. Adv. Model. Earth Syst.*, **6**, 680–699, doi:10.1002/2014MS000327.

Walsh, K., S. Lavender, E. Scoccimarro, and H. Murakami, 2013: Resolution dependence of tropical cyclone formation in CMIP3 and finer resolution models. *Climate Dyn.*, **40**, 585–599, doi:10.1007/s00382-012-1298-z.

——, and Coauthors, 2015: Hurricanes and climate: The U.S. CLIVAR working group on hurricanes. *Bull. Amer. Meteor. Soc.*, **96**, 997–1017, doi:10.1175/BAMS-D-13-00242.1.

Wehner, M. F., and Coauthors, 2014: The effect of horizontal resolution on simulation quality in the Community Atmospheric Model, CAM5.1. *J. Adv. Model. Earth Syst.*, **6**, 980–997, doi:10.1002/2013MS000276.

Zarzycki, C. M., K. A. Reed, J. T. Bacmeister, A. P. Craig, S. C. Bates, and N. A. Rosenbloom, 2016: Impact of surface coupling grids on tropical cyclone extremes in high-resolution atmospheric simulations. *Geosci. Model Dev.*, **9**, 779–788, doi:10.5194/gmd-9-779-2016.

Zhao, M., I. M. Held, S.-J. Lin, and G. A. Vecchi, 2009: Simulations of global hurricane climatology, interannual variability, and response to global warming using a 50-km resolution GCM. *J. Climate*, **22**, 6653–6678, doi:10.1175/2009JCLI3049.1.